Composites Part B 202 (2020) 108269

Contents lists available at ScienceDirect

Composites Part B

journal homepage: www.elsevier.com/locate/compositesb

Three-scale asymptotic homogenization of short fiber reinforced additively manufactured polymer composites

Aslan Nasirov [a], Ankit Gupta [a], Seymur Hasanov [a], Ismail Fidan [b,*]

[a] Tennessee Technological University, Department of Mechanical Engineering and Center for Manufacturing Research, Cookeville, TN, USA
[b] Tennessee Technological University, Department of Manufacturing and Engineering Technology, Cookeville, TN, USA

ARTICLE INFO

Keywords:
A. Polymer-matrix composites (PMCs)
B. Mechanical properties
B. Anisotropy
C. Computational modeling

ABSTRACT

In this research, prediction of mechanical properties of short fiber-reinforced composites manufactured with the help of fused filament fabrication (FFF) process is investigated. Three-scale formulation of asymptotic homogenization is employed to upscale the properties from microscale to mesoscale and from mesoscale to macroscale. Since generating microscale representative volume element (RVE) infused with short fibers requires sophisticated modeling tools, the algorithm for the microscale RVE generation is presented and discussed. Homogenization was performed for microscale RVEs with random and aligned (fibers aligned with the beads on mesoscale) fiber orientations, and for mesoscale RVEs with unidirectional and 0/90 layup formation. Tensile tests were performed for different short carbon fiber concentrations 5, 7.5 and 10% (by volume) to validate predicted homogenized properties. Moreover, to analyze the morphology of 3D printed specimens, microstructural analysis using SEM was performed on all the printed specimens. Surface morphology helped to gain more insight into the bead structure and fiber distribution. It was concluded that Young's modulus prediction using random fiber orientation has low relative errors tested in bead direction. Overall, this study has unique contribution to mechanical property prediction for FFF-made short fiber-reinforced composite parts.

1. Introduction

Additive manufacturing (AM) is a layer-by-layer manufacturing process for fabricating a wide range of structures and complex geometries with easily achievable customized features. AM has potential applications in various areas ranging from aerospace, automotive, construction and biomedical industries [21]. Based on different application areas and their specific requirements, a number of AM techniques have been developed [11] i.e. fused filament fabrication (FFF) [4], laminated object manufacturing (LOM) [35], selective laser sintering (SLS) [36], stereolithography (SLA) [38]. FFF is one of the most popular AM techniques for the fabrication of thermoplastic polymer materials. FFF process includes deposition of semi-molten material layer-by-layer through a heated nozzle in order to build three-dimensional part. Fig. 1 shows the process of depositing fiber-reinforced composite filament to build 3D part using the FFF technique. Low-cost production capability, manufacturing simplicity, customizability, etc. are some of the advantages of the FFF that have drawn the attention among industries and researchers. Nowadays, fiber-reinforced thermoplastics have been used in big area additive manufacturing (BAAM) to print large parts such as full-scale car frames printed by Oak Ridge National Laboratory (ORNL) [14,21].

However, parts produced with FFF lack strength, stiffness, thermal stability, electrical conductivity, etc. that limit its real life applications. Improving, modifying and diversifying the mechanical properties of generic materials is possible with the incorporation of fibers. Fibers can be short, long and continuous depending upon the application. Tensile, fatigue and creep properties of printed reinfroced thermoplastics have been extensively studied [25,26,31,39,42,43]. Incorporation of fibers helps in obtaining the parts of less weight, high strength, and high stiffness with minimal cost. In terms of manufacturability, short carbon fibers (SCF) are much more versatile than the long and continuous fibres and are useful in all the extrusion process with thermoplastics. Due to their low cost, SCF reinforced composites are utilized in a variety of fields and are used to enhance the performance of the printed structures [23]. In addition, SCF might be useful for achieving the isotropic property for the final composite material (CM). An accurate understanding of SCF-reinforced composites, especially in the AM process, needs to be addressed in terms of mechanics-based modeling and prediction. However, there are many challenges faced in the prediction of

* Corresponding author.
E-mail address: IFidan@tntech.edu (I. Fidan).

https://doi.org/10.1016/j.compositesb.2020.108269
Received 1 December 2019; Received in revised form 22 June 2020; Accepted 28 June 2020
Available online 28 August 2020

mechanical properties of FFF-made parts which include [7]:

(i) Anisotropy: Overall stiffness of the part varies depending on infill pattern and printing direction used. Moreover, the microstructure of the samples is highly deviated from the actual printed microstructure.
(ii) Heterogeneity: Pores and fillers cause deviation of mechanical properties in printed parts. In the case of SCF reinforced thermoplastics, voids and fibers greatly influence the mechanical properties.

It is obvious that anisotropy and heterogeneity make mechanical behavior and its prediction a complex issue in AM. This has become even more involved considering the recent transition from polymeric materials to fiber-reinforced polymers, metal-infused polymers and other complex materials. In other words, since these materials are inherently composite in nature (fiber-infused plastic and metal-infused plastic), they add another layer of complexity. Other than material, the infill pattern also plays an important role in the overall stiffness and behavior of the parts. Depending on the slicer software, different infill patterns can be generated. Therefore, the microstructure of the samples is dependent on the chosen infill pattern and needs specific mathematical models to be accounted for. For example, the unidirectional line infill with 100% infill density is shown in Fig. 2a. Fig. 2b illustrates interbead voids formed between the deposited beads. These voids reduce the mechanical properties of the printed parts resulting in anisotropic material behavior.

2. Literature review

Multiscale methods including homogenization, micromechanics and molecular dynamics have been used extensively to study properties of composite materials [45,48]. Babu et al. derived and implemented RVE generation algorithms for fiber-infused microstructures with different fiber orientations [5]. Material properties were predicted for different RVEs using asymptotic homogenization and compared to Halpin-Tsai and Mori-Tanaka methods. Belhouideg et al. determined the effective properties of the bulk metallic glass matrix composite reinforced with tungsten fiber from the microstructural description using the homogenization approaches [6]. This study concluded that relative errors between the homogenization and the experimental results were less than 10.1%. The results also showed that the shape of inclusions creates a strong influence on the mechanical properties of the final part. Islam et al. predicted the Young's modulus of polymer composites reinforced with fibers using parallel, series and Halpin-Tsai model, modified Halpin-Tsai (MHT) and Bowyer-Bader (BB) model [32]. The results of this study observed that the parallel, series and Halpin-Tsai model failed to predict the elastic modulus of the reinforced polymer while MHT and BB model gave satisfactory results. Bouaoune et al. demonstrated that random composite microstructures used in practice do not always converge to their periodic counterparts [9]. Additionally, Zerhouni et al. showed how isotorpic properties can be obtained by creating RVEs with homogeneous isotropic matrix and variable size spherical pores [62].

There is a number of studies that focused on mechanical property prediction of FFF-fabricated components. Numerous techniques such as micromechanical approaches, classical laminate theory (CLT) and analytical methods have been utilized to approximate the properties of FFF-made parts. Cuan-Urquizo et al. presented an overview of various numerical, analytical and experimental methods that were used to estimate the structural behavior of printed parts [13]. Same authors used finite element analysis (FEA), rule of mixtures and experimental data to predict Young's modulus for different infill densities [18]. Although the errors between micromechanics and simulations were negligible, the study only investigated Young's modulus in one direction. Li et al. established a micromechanics approach to calculate the orthotropic properties of laminated parts [37]. Each printed layer was modeled as a lamina while beads and voids were treated as matrix and fibers, respectively. Results of the study showed relative errors in the range of 1–16% between micromechanics and experimental results. Rodriguez et al. derived and applied similar micromechanics approximation for constitutive modeling of FFF made parts [50]. Croccolo et al. investigated the prediction of mechanical properties of samples with zero air gap between the beads [12]. The results of the predictive and experimental properties had approximately 10% difference. Domingo-Espin et al. assumed that printed parts are orthotropic instead of anisotropic and conducted experiments to calculate all orthotropic properties [15]. FEA simulations of sample parts were performed with derived orthotropic properties and isotropic properties for comparison. Error between FEA simulation of a sample part using derived orthotropic model and experimental results was less than 8%. A similar error was observed in the isotropic case and therefore study fails to present sufficient evidence that supports the application of the orthotropic material model.

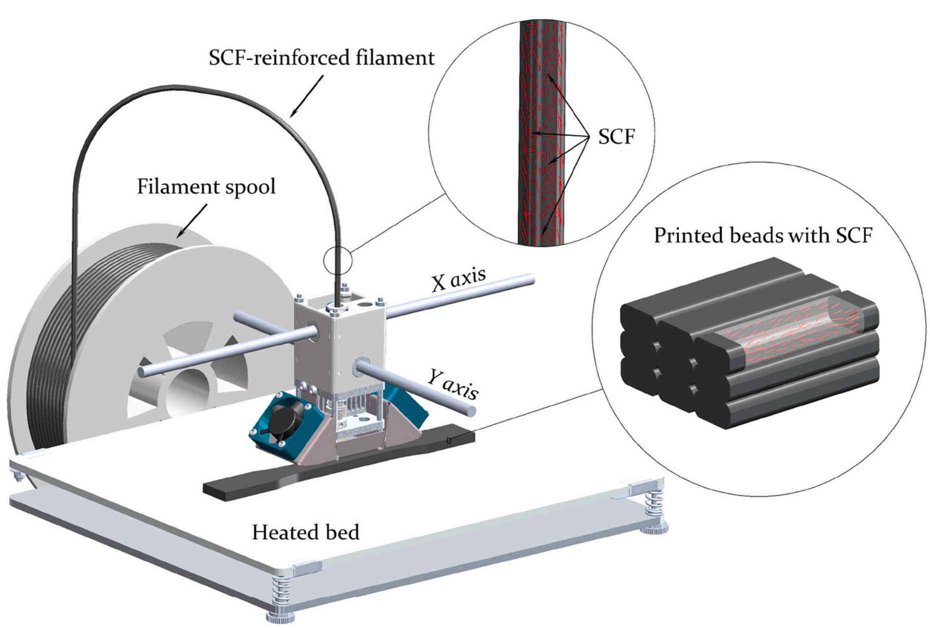

Fig. 1. Fused filament fabrication of SCF reinforced composites.

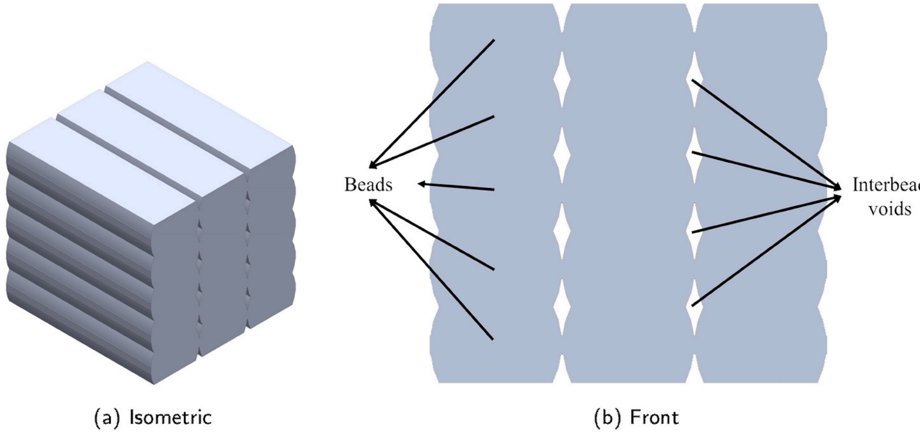

Fig. 2. Interbead voids in printed part a) Isometric view b) Front view.

Somireddy et al. presented a finite element procedure to find elastic moduli of a layer of the FFF processed part [54]. Properties obtained from FEA simulations were used as an input into CLT that was used to estimate homogenized property for the entire printed structure. The layers in the study were treated as a unidirectional laminate structure. Effective laminate properties were compared to experimental data, and relative errors were lower than 5%. Biswas et al. conducted a computational study based on microstructural information of 3D-printed parts using micromechanics approach based on RVE [8]. Micro-CT data and periodic geometry for RVE with various raster angles were used in FEA models. Although experimental results showed some fluctuations, there was an agreement between numerical and experimental results. Moreover, Ngo et al. studied bimaterial bio-inspired composites under different loading conditions using FEA [44]. FEA results showed how cohesive/adhesive layers mitigate impact loads and minimize plastic damage to composite structures.

As for the printed composites, Moumen et al. summarized the latest works on modeling aspects of printed composites [41]. Dutra et al. studied the prediction of mechanical properties of printed parts with continuous carbon fiber reinforcement [16]. However, uncertainty in Young's modulus of nylon hindered the accurate prediction of properties and only modulus values higher than 3 GPa yielded accurate prediction. Wang et al. studied the prediction of mechanical properties of SCF-reinforced printed composite parts [57]. In their study, the fiber orientation was predicted after the deposition process. The fiber orientation distribution function was used to predict the resulting mechanical properties using the averaging technique. This study was focused on numerical simulations and lacks experimental benchmarking. Fiber orientation prediction was mainly studied for simulation of injection molding and has been studied both in theoretical [27] and applied [3] context. Recent work by Somireddy et al. studied the prediction of Young's modulus for cross-ply and angle-ply printed laminates [55]. Experimentally measured modulus for single ply is used as an input to CLT. Errors varied between thin and thick plates and were less than 20%, in general. However, this approach lacks fundamental understanding of the hierarchical structure and mechanics of printed SCF-reinforced composites. Papon et al. predicted mechanical properties of 3D printed composites using non-intrusive polynomial chaos (NIPC), rule of mixtures and classical laminate theory [47]. Study accounted for stochastic effects on both micro and macro scales and analytical results showed good agreement with experimental trends.

As mentioned before, the hierarchical/multiscale structure of printed composite has to be considered in the mathematical model. Although FFF-printed polymers have been studied vastly in recent years, property prediction of fiber-reinforced composites has not been investigated yet. The research study reported in this paper focuses on the application of three-scale asymptotic homogenization for the prediction of mechanical properties of FFF-made SCF reinforced specimens. Three-scales are employed to account for macroscale geometry, mesoscale voids and microscale reinforcements. Hierarchical structure allows for flexibility in separating the scales and controlling each one of them independently from the others. Experimental results were employed to validate and benchmark the homogenized properties compared to the real behavior of the parts.

3. Material and methods

3.1. Computational methods

3.1.1. Asymptotic homogenization

Multiscale modeling techniques primarily consist of homogenization methods that focus on finding effective material properties thus substituting heterogeneous part with an equivalent homogenized one. Another family of multiscale methods enriches kinematical relationships to capture microstructural effects. Due to the periodic nature (ideally) of the infills and lattice structures used in FFF, homogenization methods are applicable as a multiscale modeling tool for FFF-made parts. Examples of different homogenization methods include statistical homogenization, heterogeneous multiscale method (HMM), asymptotic methods, Hill-Mandel macrohomogeneity condition, generalized method of cells, FEA based methods and etc. [22,33,34,46,53,61]. In this study, asymptotic homogenization (AH) is employed due to its extendability to multiple length scales and ability to model hierarchical structures. This is crucial to this study since SCF-reinforced printed specimens have three-scale hierarchy. Therefore, most of the micromechanics or homogenization methods that are limited to two scales would not be applicable to printed SCF-reinforced composites. Moreover, since partial differential equations derived from asymptotic analysis can be solved using the finite element method, AH can be applied to complex geometries. AH predicts homogenized properties of a heterogeneous part from material properties of the constituents and RVE geometry. Microscale stresses, strains, and deformations can also be predicted at specific nodes/integration points in the macroscale domain. AH can also be further developed to capture nonlinearities, multiple scales and other complex phenomena. Therefore, the application of AH was explored in this study as a homogenization tool for FFF-made parts. Derivation of the equilibrium equations and finite element formulation are presented in Appendix A.

3.1.2. Microscale RVE generation

RVE generation for microstructures with a high number of inclusions is a long-standing challenge. Thomas et al. summarized and compared the existing RVE generation algorithms [56]. The main limitation in most of the reported algorithms is that there is a limit for achievable fiber concentration with a given aspect ratio (AR). Fiber AR is equal to the ratio of fiber length to fiber diameter. In present study, nominal AR is approximately equal to 14 [2]. In other words, it becomes harder to accommodate more fibers to the RVE as the number of fibers increases. In this research, concentrations are relatively low, even though fiber AR is high. However, typically fiber length after extrusion is different from the nominal length because of the fiber breakage due to fiber-to-fiber interaction, and fiber contact with extruder lead screw threads. In order to get the actual size of the fibers after filament extrusion, thermogravimetric analysis (TGA) was performed at 800° C° to degrade all the PLA material of the sample filament leaving behind only SCF. Measured fiber length was equal to 60 μm on average for 5% concentration. Therefore, the fiber length used in the RVE generation was 60 μm. Detailed algorithm for microscale RVE generation is given in Appendix B.

All the generated RVEs are shown in Fig. 3. RVEs were generated for 5, 7.5, and 10% for both random (Fig. 3a,b,c) and aligned distributions (Fig. 3d,e,f). For random distribution, all fibers had uniform random orientation assigned to them. For the aligned distribution, fibers were perfectly aligned with bead direction on the mesoscale. The size of RVE is also crucial to obtain consistent properties. For random distribution, RVE size should be large enough to achieve a quasi-isotropic behavior. By quasi-isotorpic behavior it is meant that orthotropic terms in stiffness matrix resemble isotropic material behavior while overall stiffness matrix is anisotropic. After several trials, 0.200 mm X .200 mm X .200 mm box size was found sufficient to obtain quasi-isotropic behavior. Obviously, parameters like simulation time and mesh size increase as RVE size increases. As a result, RVE size should be as small as possible while predicting quasi-isotropic behavior as mentioned before. However, for aligned distribution, RVE size does not make much difference since it is clear that the orientation is not random and stiffness matrix is going to be approximately transversely isotropic. Therefore, RVEs were constructed with 0.100 mm X .100 mm X .100 mm box size. Concept of quasi-isotropy is illustrated in Eq. (42) which shows homogenized stiffness matrix for microscale RVE infused with randomly distributed SCF (5% concentration). $D(1,1), D(2,2), D(3,3)$ terms are almost equal to each other. The same pattern is observed for $D(4,4), D(5,5), D(6,6)$ and $D(2,1), D(3,1), D(3,2)$. The rest of the terms in the stiffness matrix stand for anisotropic coupling. If anisotropic coupling terms are ignored then stiffness matrix becomes almost isotropic. For comparison, Eq. (43) represents stiffness matrix for microscale RVE infused with aligned CF (5% concetration). In this case, the only difference is that $D(3,3)$ term is higher than $D(1,1), D(2,2)$ because fibers are aligned with the Z direction.

3.1.3. Numerical experiments

In this study, both homogenization and experimental results were obtained for two cases: unidirectional (UD) and 0/90 layup. These two cases were chosen because tensile experiments can only be performed for balanced symmetric laminates due to tension-shear, tension-bending, and tension-torsion coupling. Homogenization was performed for ideal mesoscale RVEs shown in Fig. 4. Ideal RVE corresponds to the RVE modeled according to the microstructure obtained from the slicer software tool (Cura). Ideal RVEs were studied to assess the prediciton of mechanical properties straight from Cura without the need for microstructural images. Constituent material properties of fiber and matrix are given in Table 7. Since anisotropy in mechanical properties of carbon fibers has low effect on the macroscale properties, carbon fibers were assumed to be isotropic for the sake of simplicity. Since the goal of this study was to predict the mechanical properties in different directions, specimens were printed in the 0, 90, 0V and 0/90, 0/90/V. Specimen name coding is explained in Fig. 4 with testing and printing directions shown using arrows. In the UD case, 0 stands for samples printed with all beads aligned with the tensile force direction during the tensile tests, 90 stands for samples printed with all beads transverse to the tensile force direction during the tensile tests and 0V stands for samples printed and tested in vertical direction. In the 0/90 layup, 0/90 stands for samples printed with 0/90 layup and tested in bead direction, and 0/90V stands for samples printed with 0/90 layup and tested in vertical direction. Since 90/0 would be exactly equal to 0/90, 90/0 layup was not studied. Additionally, actual RVEs, given in Fig. 4c and d, were studied to assess influence of actual printed microstructure on the homogenized properties. Actual RVE was modeled according to microstructural images given in Fig. 5. Actual RVE was randomly selected from microstructure, processed using ImageJ image processing software and remodeled in SolidWorks.

3.2. Experimental setup

A single nozzle 3D printer was used to fabricate the polymer matrix composite (PMC) material with SCF reinforcement. Table 2 shows the processing parameters employed for the printing process. Fig. 6 shows the schematic view of the entire fabrication process used in producing the polylactic acid (PLA)/SCF composite material. The setup includes

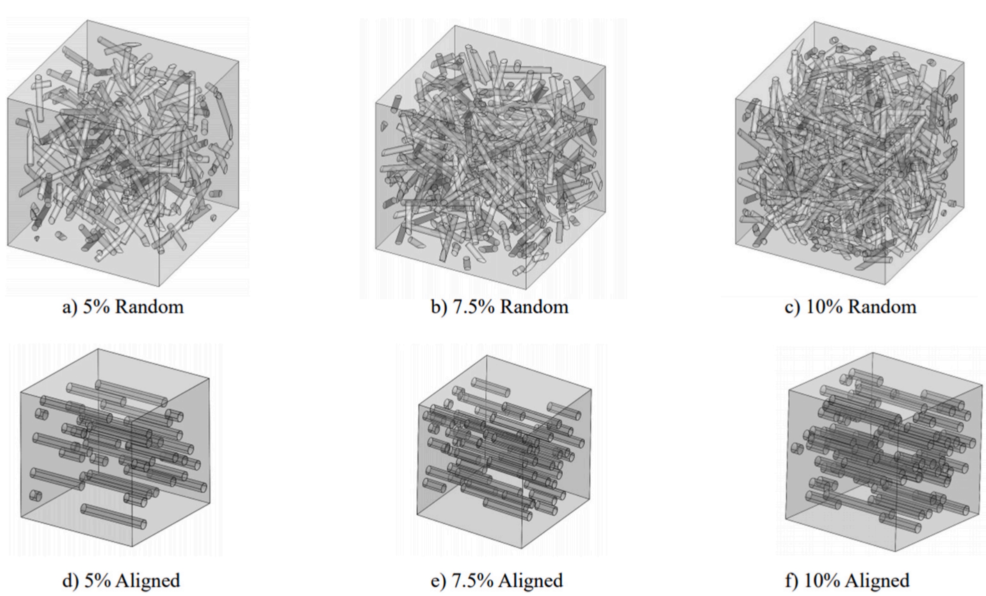

Fig. 3. Generated RVEs for various SCF concentrations and random and aligned orientations.

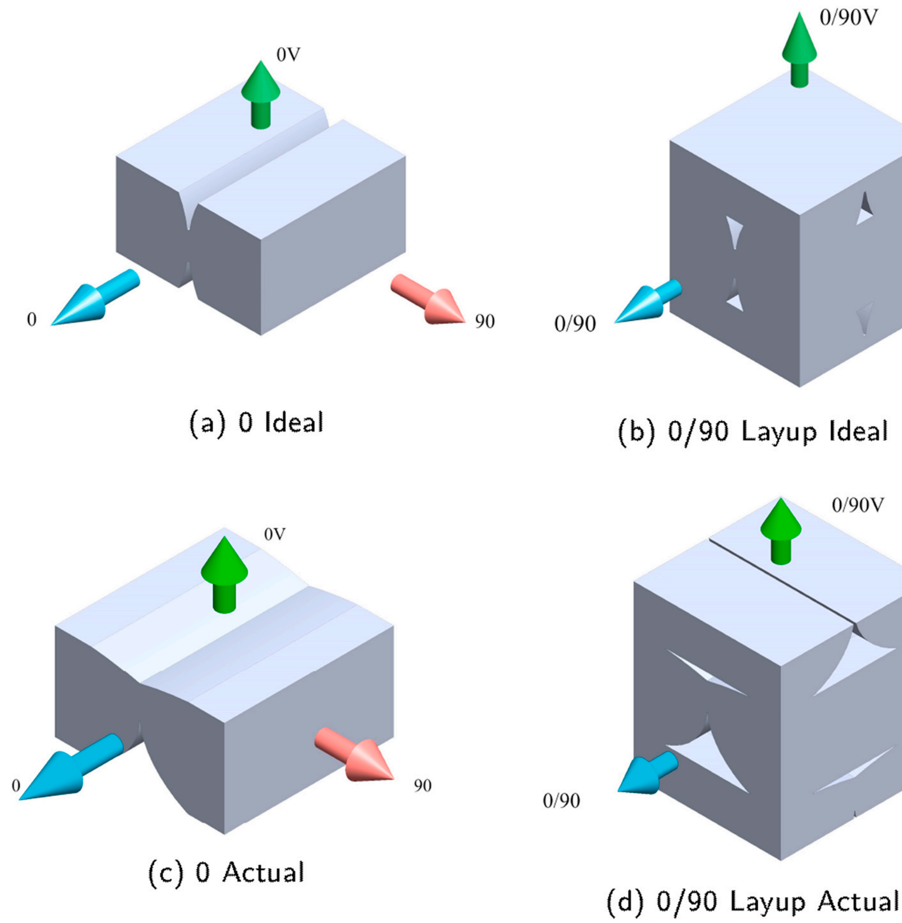

Fig. 4. Mesoscale RVEs for a) UD b) 0/90 layup c) Actual RVE UD d) Actual RVE 0/90.

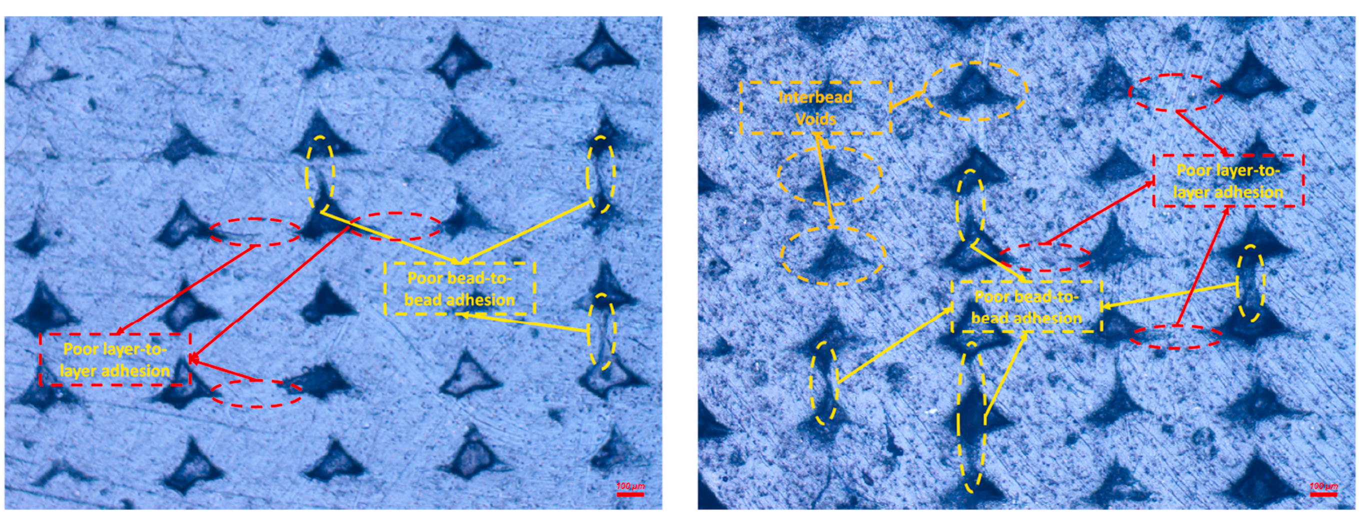

Fig. 5. Mesostructural images with indication of poor adhesions and interbead voids.

the air path, extruder with 2.85 mm diameter hardened steel nozzle, filament spooler and 3D printer. PLA pellets are dried in a furnace, extruded and printed using Ultimaker 5. Table 1 shows the filament extrusion parameters i.e. extrusion speed, extrusion temperature and air path speed. Extrusion parameters were carefully adjusted to achieve a uniform diameter of the composite filament.

3.2.1. *Material selection*

PLA as the matrix material from 3DXTech and SCF as the reinforcement from ZOLTEK were used to fabricate the 3D printed CM. PLA is a low-cost biodegradable material which makes it the first choice in various applications like bottles, plastic films, aesthetic models, jigs and fixtures, biodegradable medical devices (pins, screws, rods, plates, etc). The low printing temperature and outstanding surface finish make it an ideal 3D printing material. SCF are infused inside the PLA matrix to

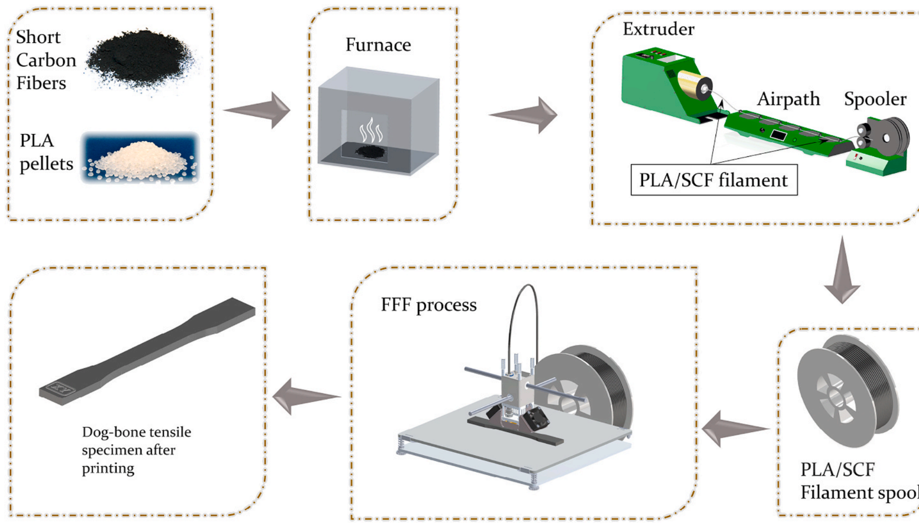

Fig. 6. Process chart for fabricating SCF-reinforced composites.

Table 1
Filament extrusion process parameters.

Properties	Values
Extrusion Temperature (°C)	215
Air Path Speed (m/sec)	30
Extrusion Speed (mm/sec)	25
Filament Diameter (mm)	2.65–2.85

Table 2
Printing process parameters.

Properties	Values
Bed Temperature (°C)	50
Extrusion Temperature (°C)	215
Infill Density (%)	100
Infill Pattern	Line
Layer Thickness (mm)	0.3
Printing Speed (mm/sec)	30
Number of shell/top/bottom layers	0
Cooling Fan (%)	100

widen the applicability of the resulting CM. High stiffness, high tensile strength, low thermal expansion, and low weight are some of the properties of SCF that makes them useful as reinforcement. Printed CM reinforced with SCF are cheap, easy to manufacture, commonly available and useful in the fabrication of any type of complex structures that are not feasible to manufacture with continuous carbon fibers.

3.2.2. Experimental procedure

All the experiments were performed using PLA as the matrix material and SCF (having nominal length 100 μm and diameter 7.2 μm) as the reinforcement. Using PLA and SCF, three mixtures were prepared by mixing them thoroughly according to the following volume fraction of SCF 95% PLA +5% SCF (by vol.), 92.5% PLA + 7.5% SCF (by vol.) 90% PLA + 10% SCF (by vol.). The prepared mixtures were poured into the filament extruder for the composite filament generation. Table 1 shows the filament extrusion parameters. Vernier caliper was used to check the uniformity of the diameter simultaneously while extruding. Finally, extruded PLA/SCF composite filament was used to fabricate the PMC samples. The entire procedure was repeated to generate the rest of the samples with different concentrations. Tensile properties of PLA/SCF were examined using the universal testing machine (UTM-INSTRON 5582). Tensile testing was conducted in accordance with ASTM D638 Type I with 5 mm/min strain rate and gauge length of 50 mm. Two samples were printed and tested for each SCF concentration.

4. Results and discussion

A number of trial experiments were performed to investigate the feasibility of using the SCF-reinforced PLA. SCF should have significant adhesion with PLA polymer to improve the mechanical performance of the final CM. To check the adhesiveness of these materials, SEM analysis was performed to observe the interface between fiber and matrix. After the investigation, it was found that SCF can be used as the reinforcing material with PLA material because of the significant adhesion as shown in Fig. 7.

4.1. Microstructural analysis

In order to analyze the microstructure of the 3D printed parts, small samples with dimensions 10 mm × 10 mm × 10 mm were printed. These samples were cut from two faces with the help of a diamond saw cutter to obtain the side and cross-sectional view of the CM. Polishing was done with silicon carbide emery papers to achieve the mirror finish. Excess polymer material from the surface of the carbon fibers was removed using potassium permanganate etching (Sulfuric acid – 50 ml, Ortho-phosphoric acid – 20 ml, Distilled water – 5 ml and Potassium permanganate – 0.55 g) to get clear images of embedded fibers inside the PLA matrix. Fig. 7 shows the SEM images of the SCF-reinforced PLA matrix (10% by vol.). From the figure, it is concluded that there is no fiber agglomeration and the fibers are uniformly distributed inside the PLA matrix which eventually helps in enhancing the stiffness values of the final CM. It should be noted that extruded filaments were re-extruded to unifromly distribute fibers throughout the filament.

4.2. Experimental results

As mentioned before, the tensile specimens were printed with the specimen codes as shown in Fig. 4 for all SCF concentrations. Table 3 shows the experimental results in all directions. Stress-strain curves for all volumetric fraction and orthotropic directions are given in Fig. 8. From the table, it can be observed that the elastic modulus increases with increase in fiber concentration inside the PLA samples printed in 0 and 0/90 directions. This trend is not consistent for the samples printed in other directions. The reason of this behavior could be related to poor bead-to-bead and layer-to-layer adhesion as shown in Fig. 5. Since the SCF used in making the 3D printed CM are stiffer than the PLA

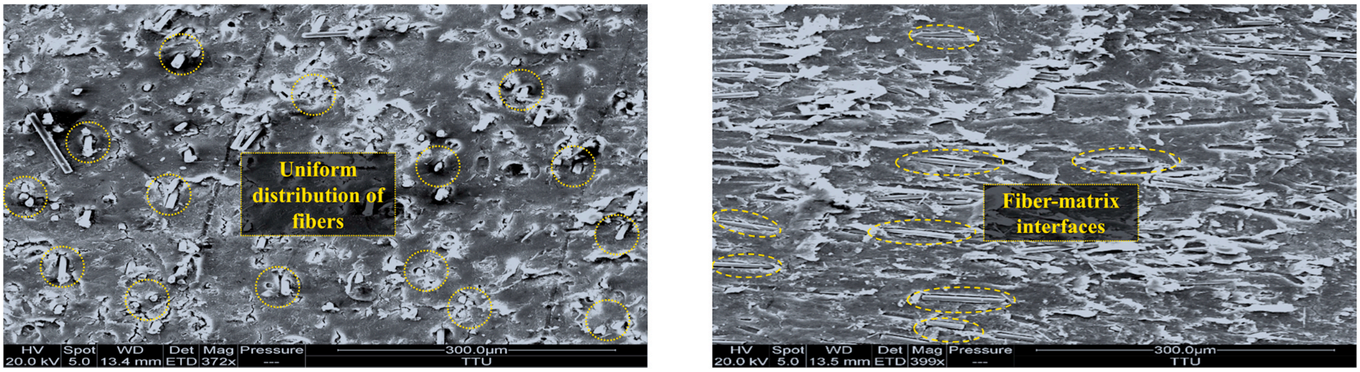

Fig. 7. SEM images showing the interface and uniform fiber distribution for SCF (10% by vol)/PLA

Table 3
Testing results for SCF reinforced specimens.

Direction	5%			
	Young Modulus (GPa)	Standard Deviation	Tensile Strength (MPa)	Standard Deviation
0	4.418	0.186	39.486	1.232
90	2.180	0.213	12.708	2.418
0 V	2.741	0.191	25.376	0.726
0/90	3.501	0.100	31.534	2.631
0/90/V	2.396	0.165	17.338	5.704
Direction	7.5%			
0	4.573	0.035	33.422	4.434
90	2.966	0.536	30.461	7.156
0 V	2.412	0.143	16.037	0.632
0/90	3.382	0.065	26.344	0.611
0/90/V	2.194	0.366	16.887	0.101
Direction	10%			
0	5.223	0.131	38.259	3.438
90	2.463	0.251	23.332	2.361
0 V	3.458	0.272	30.893	0.440
0/90	3.916	0.124	26.350	2.756
0/90/V	2.476	0.214	17.426	5.920

polymer, they have the tendency to restrict the movement of polymer chains in the proximity of other chains resulting higher stiffness of the final part than the neat PLA. Maximum Young's modulus achieved was approximately 150% of the neat PLA. There is evident anisotropy in strength and stiffness properties over the tested directions. This has also been concluded in numerous studies on 3D printed parts [4,17].

Tensile strength did not increase consistently with increase in fiber concentration. Furthermore, the tensile strength of the reinforced-PLA was less than the neat PLA in all directions because of the formation of local stresses inside the specimen. Stress concentrations form due to both mesoscale voids and fibers. Microscale normalized Von Mises stresses under loading in X direction is shown in Fig. 9. It is seen that stresses are concentrated at the sharp corners of the RVE. Fig. 7 shows that the SCF inside the PLA material are not perfectly aligned. As the tensile load is applied, fibers start acting as the stress concentrators resulting in the formation of local stresses. These local stresses initiate cracks that propagate at the interface of two materials and result in matrix cracking.

4.3. Homogenization results

4.3.1. Ideal RVE

Overall, three-scale hierarchy showing workflow from micro to macroscale is shown in Fig. 10. Since orientation of fibers was not found experimentally, it was assumed as random and aligned with the beads. As mentioned before, ideal and actual mesoscale RVEs were studied to understand mesostructure. Therefore, first, ideal mesoscale RVE with random and aligned fiber orientation was investigated. A comparison of experimental and homogenized results are given in Table 4. It is clear from Table 4 that homogenization errors for 0 direction are under 10%. However, high errors are observed in 90 direction and vertical samples. Similarly, it is evident that the relative errors for the 0/90 direction are around 10%–20%. On the other hand, comparative errors in predicted modulus for 0/90/V are more than 50%. As in UD case, predictions of moduli for vertically printed samples have relative errors higher than 40%. Therefore, the errors for samples printed in 0 and 0/90 directions are low while for 90 and vertically printed samples have significant errors. As mentioned in Section 4.2, one possible reason for high errors in transverse and vertical directions is poor layer-to-layer and bead-to-bead adhesion, as shown in Fig. 5.

As for microscale RVEs with aligned fiber orientations, a comparison between experimental and homogenized results is given in Table 4. As the results present, properties are overestimated for all directions by a high margin. Fig. 7 shows that the SCF inside the PLA material are not perfectly aligned. Therefore, perfectly aligned fiber orientation assumption is innacurate in this case. Similarly, Somireddy et al. performed CT-scanning and concluded that fibers are not perfectly aligned with the printing direction [55].

4.3.2. Actual RVE

Homogenized properties for actual RVE are given in Table 5. Since aligned fiber orientation results in dramatically high errors, only random fiber orientation was used for simulations with actual RVE. It can be seen that errors in 0 samples are slightly higher (<15%) while errors for 90 and 0V have improved significantly. Similarly, errors in 0/90 directions and 0/90 V directions have improved. It is worth noting that 0 and 0/90 directional properties are relatively easy to accurately predict while prediction of 90 and vertical directional properties still remains a challenge. Moreover, since actual RVE was randomly picked from microstructure, properties derived from it do not necessarily represent the average properties over the microstructure. This can explain the variations of the properties in 90 and vertical directions. Overall, it clear that random orientation yields better prediction than aligned orientation. The same conclusion was reached by Heller et al. who modeled flow thorugh the nozzle in the FFF process [10,29,30]. Results revealed that die swell effect decreases the fiber alignment upon nozzle exit and therefore fibers are not perfectly aligned throughout the bead. Note that while deriving properties for actual RVE and random fiber orientations, all the anisotropy was ignored. In other words, anisotropic material behavior was reduced to orthotropic behavior to extract orthotropic material properties.

For completeness, homogenized properties derived for all RVEs are shown in Table 6. Axis 3 is the axis along the bead, axis 2 is the vertical axis and axis 1 is the transverse axis. Homogenized Young's moduli and shear moduli steadily increase for all cases while Poisson's ratio stays roughly the same. Furthermore, moduli values for ideal RVEs are higher than actual RVE as expected.

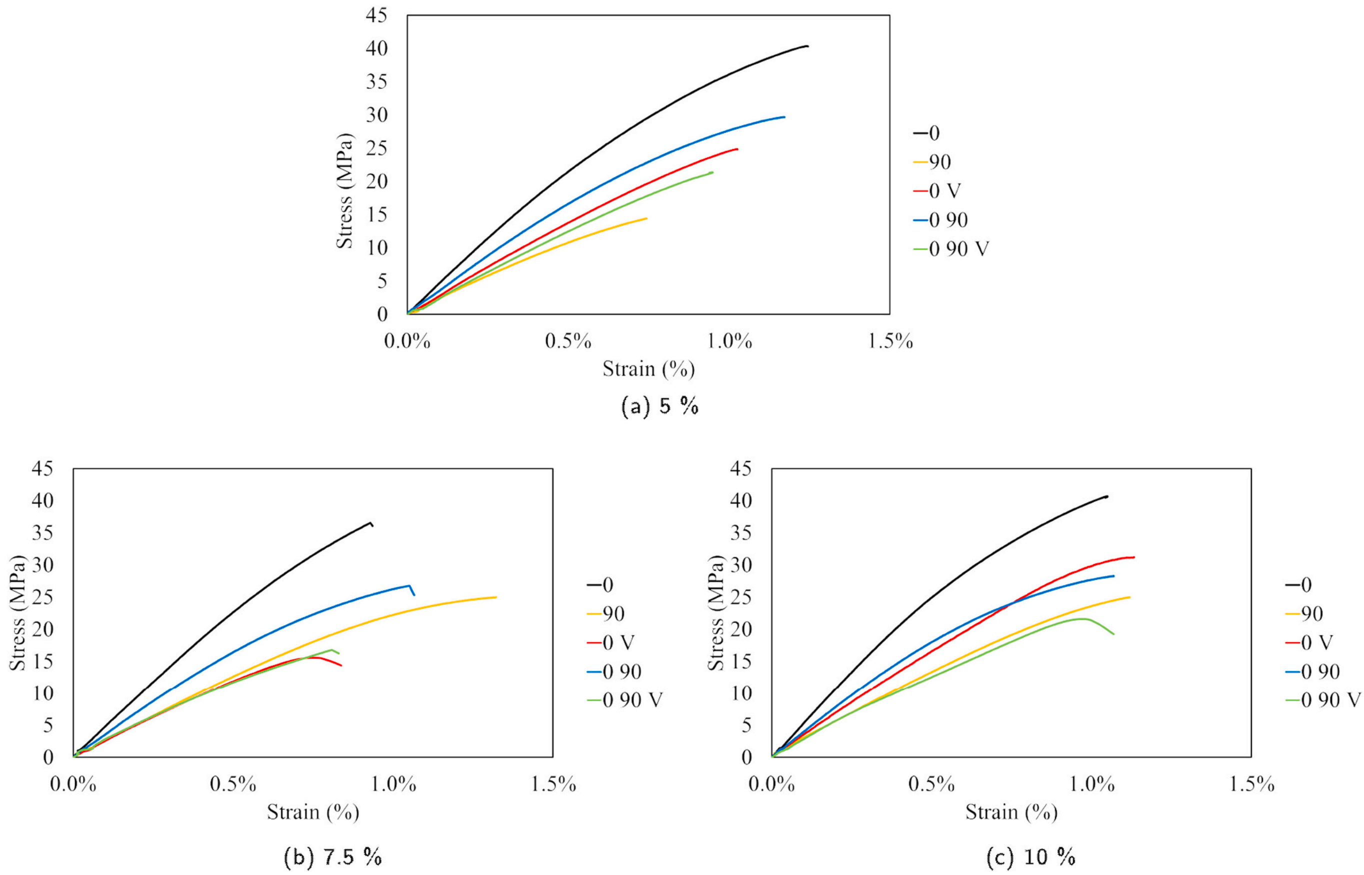

Fig. 8. Stress-strain curves for a) 5% b) 7.5% and c) 10%.

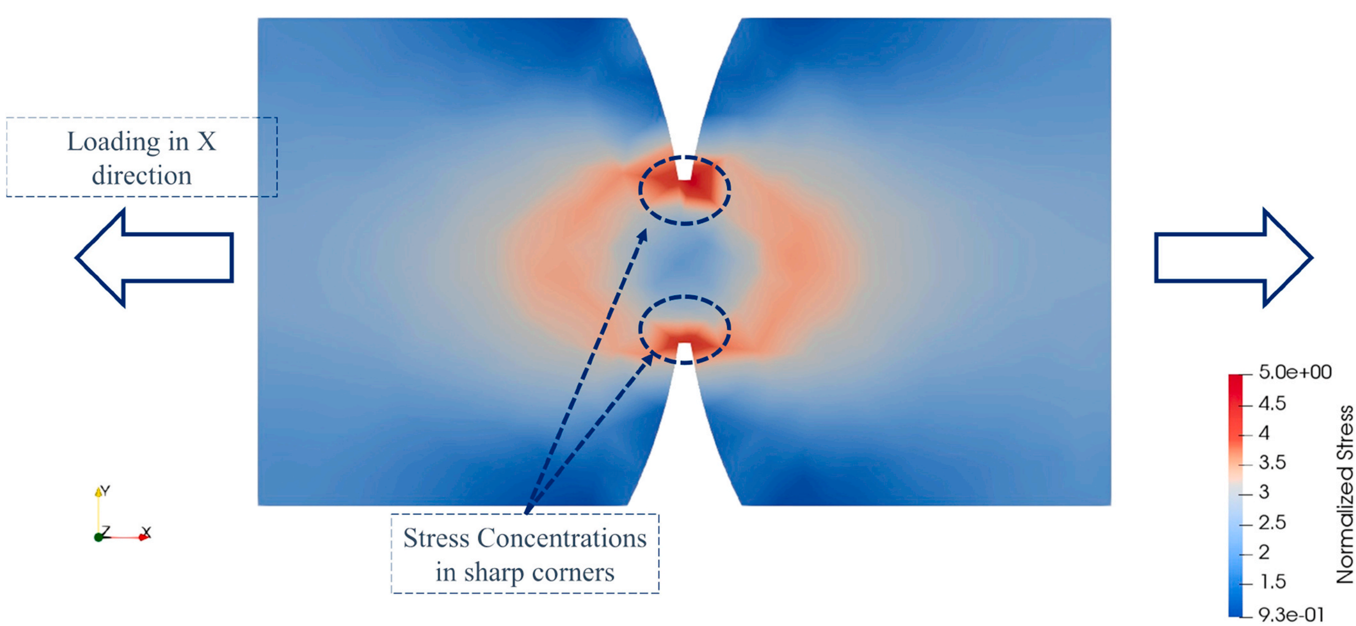

Fig. 9. Microscale normalized Von Mises stress fields.

5. Conclusion

The present research study focuses on the numerical prediction of mechanical properties of the FFF-made SCF-reinforced PLA specimens. Mechanical properties were predicted using three-scale asymptotic homogenization for both random and aligned fiber distributions in five different directions i.e. 0, 90, 0V, 0/90, 0/90V. Mechanical behavior of the 3D printed samples was also studied experimentally. FFF technique was used to fabricate the SCF-reinforced PLA composite specimens. Mechanical properties and surface characteristics were investigated. Then, homogenized properties were compared to experimental results. After experimental investigation, the following points were concluded:

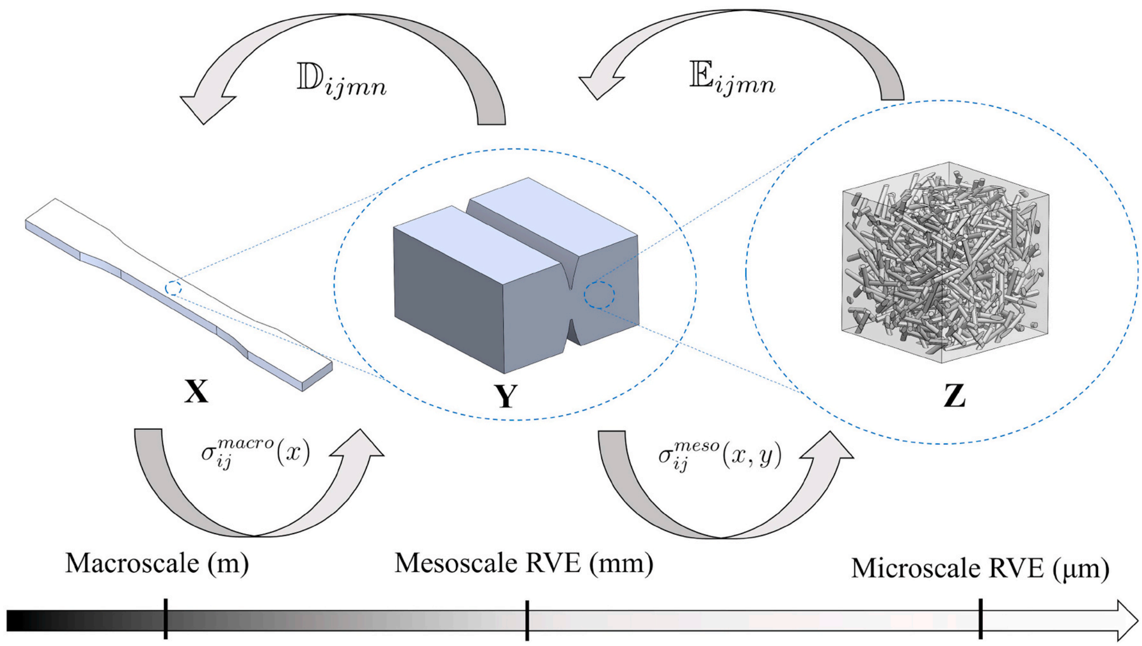

Fig. 10. Macroscale, mesoscale and microscale domains and three-scale hierarchy.

Table 4
Comparison between experimental results and homogenized results for ideal RVE.

Concentration	Modulus Direction	Experimental Young's modulus (GPa)	Standard Deviation	Homogenized Random Orientation		Homogenized Aligned Orientation	
				Homogenized Young's modulus (GPa)	Error (%)	Homogenized Young's modulus (GPa)	Error (%)
5%	0	4.418	0.186	4.150	6.048	6.389	44.408
5%	90	2.180	0.213	3.120	43.119	2.834	28.852
5%	0V	2.741	0.191	4.078	48.748	3.833	39.811
5%	0/90	3.501	0.100	3.881	10.882	4.884	39.512
5%	0/90 V	2.396	0.165	3.996	66.759	3.829	59.802
7.5%	0	4.573	0.035	4.444	2.822	7.992	74.756
7.5%	90	2.966	0.536	3.404	14.772	3.031	2.211
7.5%	0 V	2.412	0.143	4.388	81.939	4.110	70.413
7.5%	0/90	3.382	0.065	4.195	24.042	5.826	72.288
7.5%	0/90V	2.194	0.366	4.299	96.004	4.156	89.453
10%	0	5.223	0.131	4.932	5.563	9.705	85.814
10%	90	2.436	0.251	3.689	49.753	3.204	30.056
10%	0 V	3.458	0.272	4.901	41.740	4.334	25.360
10%	0/90	3.916	0.124	4.602	17.529	6.797	73.572
10%	0/90 V	2.476	0.214	4.801	93.941	4.440	79.359

Table 5
Comparison between experimental results and homogenized results for actual RVE.

Concentration	Modulus Direction	Experimental Young's modulus (GPa)	Standard Deviation	Homogenized Random Orientation	
				Homogenized Young's modulus (GPa)	Error (%)
5%	0	4.418	0.186	3.804	13.888
5%	90	2.180	0.213	2.697	23.721
5%	0V	2.741	0.191	2.491	9.134
5%	0/90	3.501	0.100	3.227	7.814
5%	0/90 V	2.396	0.165	1.434	40.156
7.5%	0	4.573	0.035	4.073	10.941
7.5%	90	2.966	0.536	2.942	0.797
7.5%	0 V	2.412	0.143	2.680	11.116
7.5%	0/90	3.382	0.065	3.488	3.142
7.5%	0/90V	2.194	0.366	1.543	29.657
10%	0	5.223	0.131	4.520	13.457
10%	90	2.463	0.251	3.188	29.425
10%	0 V	3.458	0.272	2.994	13.695
10%	0/90	3.916	0.124	3.825	2.319
10%	0/90 V	2.476	0.214	1.715	30.727

Table 6
Orthotropic homogenized properties obtained from simulations.

RVE Layup	Property	Ideal RVE random			Ideal RVE Aligned			Actual RVE Random		
		5	7.5	10	5	7.5	10	5	7.5	10
0	E1 (Gpa)	3.120	3.404	3.689	2.834	3.031	3.204	2.697	2.942	3.188
	E2 (Gpa)	4.078	4.388	4.901	3.833	4.110	4.334	2.491	2.680	2.984
	E3 (Gpa)	4.150	4.444	4.932	6.389	7.992	9.705	3.804	4.073	4.520
	NU12	0.265	0.269	0.256	0.320	0.327	0.334	0.222	0.226	0.215
	NU13	0.252	0.255	0.247	0.156	0.133	0.116	0.237	0.240	0.233
	NU23	0.343	0.338	0.336	0.213	0.179	0.154	0.229	0.225	0.223
	G23 (Gpa)	1.603	1.701	1.948	1.382	1.468	1.550	1.108	1.179	1.345
	G31 (Gpa)	1.315	1.434	1.590	1.146	1.218	1.310	1.174	1.280	1.420
	G12 (Gpa)	1.405	1.541	1.679	1.189	1.247	1.322	0.964	1.056	1.148
0/90	E1 (Gpa)	3.923	4.279	4.642	4.886	5.829	6.800	3.264	3.560	3.860
	E2 (Gpa)	3.996	4.299	4.801	3.829	4.156	4.440	1.434	1.543	1.715
	E3 (Gpa)	3.840	4.111	4.563	4.882	5.824	6.794	3.190	3.415	3.790
	NU12	0.322	0.326	0.310	0.371	0.377	0.382	0.283	0.287	0.273
	NU13	0.314	0.317	0.309	0.241	0.216	0.197	0.275	0.279	0.271
	NU23	0.338	0.333	0.331	0.291	0.269	0.250	0.128	0.127	0.125
	G23 (Gpa)	1.520	1.613	1.844	1.300	1.375	1.454	0.707	0.754	0.853
	G31 (Gpa)	1.431	1.564	1.730	1.246	1.325	1.424	1.183	1.292	1.430
	G12 (Gpa)	1.529	1.679	1.829	1.300	1.375	1.454	0.714	0.782	0.851

- SCF are uniformly distributed inside the PLA based CM with sufficient adhesion between the fibers and matrix to create a significant influence on the final mechanical properties of the specimens.
- SCF are not perfectly aligned in the printing directions i.e. oriented at some angle with respect to printing directions.
- Young's modulus in 0 and 0/90 directions constantly increases up to 1.5 times modulus of neat PLA. However, decrease in tensile strength was observed after fiber reinforcement.

Using the asymptotic homogenization approach, the following points were concluded:

- In case of random fiber orientation, relative errors were low in the direction of beads for unidirectional case and 0/90 layup case ($\sim$20%). However, relative errors were high for transverse direction and vertically printed cases ($>$40%). Suggested reason for this is inconsistent layer-to-layer and bead-to-bead adhesion. As for the aligned fiber orientation, homogenized results showed significant error percentages in all directions ($>$28%). Therefore, random fiber orientation yields better predictions than aligned fiber orientation.
- Using actual RVE, relative errors were improved significantly. Errors in 0, 0V, 0/90 were less than 20% while errors for 90 and 0/90V were less than 40%. This proves that influence of actual microtructure is substantial on mechanical properties and is far from ideal.

6. Future work

As a continuation of the current work the following possible contributions could be made:

- Predicting or experimentally measuring the fiber length/orientation distribution to improve the accuracy of numerical predictions is a potential research study to follow-up on the current research results. Fiber length distribution (that was assumed constant in this study) changes with changing concentration and should be measured experimentally or theoretically. Computed tomography could be employed as an experimental technique to measure fiber orientation distribution [59] or segmentation methods that reconstruct 3D models from 2D micrographs could also be used [40]. For theoretical predictions, different fiber orientation prediction models obtained for injection molding and BAAM could be employed to find the fiber orientation distribution function [3].
- Furthermore, microscale voids can be characterized and included in microscale generation algorithms. As for mesoscale microstructure representation, since mesoscale actual RVE was randomly selected in this study, in general it can be averaged over the microstructure to achieve more accurate results.
- The input properties at layer-to-layer and/or bead-to-bead interfaces are not clearly understood. Predicting or experimentally measuring interface properties could improve the accuracy of the existing models. Moreover, the fiber-matrix interface could be modeled using imperfect interfaces.

CRediT authorship contribution statement

Aslan Nasirov: Conceptualization, Investigation, Software, Methodology, Validation, Resources, Formal analysis, Data curation, Writing - original draft, Writing - review & editing. **Ankit Gupta:** Investigation, Resources, Data curation, Writing - original draft, Writing - review & editing. **Seymur Hasanov:** Investigation, Resources, Data curation, Writing - original draft, Writing - review & editing. **Ismail Fidan:** Conceptualization, Resources, Data curation, Supervision, Project administration, Writing - review & editing.

Declaration of competing interest

We wish to confirm that there are no known conflicts of interest associated with this publication and there has been no significant financial support for this work that could have influenced its outcome.

Acknowledgements

This work was supported by the National Science Foundation [NSF Award Number 1601587]. Support provided by Wayne Hawkins of the Center of Manufacturing Research and Dr. Ben Mohr of Civil and Environmental Engineering Department is greatly appreciated.

A. Three-scale asymptotic homogenization

AH is based on asymptotic expansion of primary field (displacement field in case of elasticity) over macroscopic and microscopic domains [24,28,49,52]. Similar to the two-scale case, displacement field is expanded in three scales as follows

$$u^{\varepsilon}(x) = u(x,y,z) \approx u^{(0)}(x) + \varepsilon u^{(1)}(x,y) + \varepsilon^2 u^{(2)}(x,y,z) + \varepsilon^3 u^{(3)}(x,y,z) + H.O.T. \tag{1}$$

where x is macroscale position vector defined over macroscale domain X, y is mesoscale position vector defined over RVE domain Y and z is microscale position vector defined over RVE domain Z. H.O.T. stands for higher order terms that were ignored in this study. It should be noted that leading order term is independent of both y and z, first order term is independent of z. Strain tensors at various scales are given by

$$\varepsilon_{ij}^{micro}(x,y,z) = u^{(0)}_{(i,x_j)}(x) + u^{(1)}_{(i,y_j)}(x,y) + u^{(2)}_{(i,z_j)}(x,y,z) \tag{2}$$

$$\varepsilon_{ij}^{meso}(x,y) = \frac{1}{|Z|}\iiint_Z \varepsilon_{ij}^{micro}(x,y,z)\, dZ \tag{3}$$

$$\varepsilon_{ij}^{macro}(x) = \frac{1}{|Y|}\iiint_Y \varepsilon_{ij}^{meso}(x,y)\, dY \tag{4}$$

and stress tensors at various scales are given by

$$\sigma_{ij}^{micro}(x,y,z) = \mathbb{C}_{ijkl}(z)\varepsilon_{kl}^{micro}(x,y,z) \tag{5}$$

$$\sigma_{ij}^{meso}(x,y) = \frac{1}{|Z|}\iiint_Z \sigma_{ij}^{micro}(x,y,z)\, dZ \tag{6}$$

$$\sigma_{ij}^{macro}(x) = \frac{1}{|Y|}\iiint_Y \sigma_{ij}^{meso}(x,y)\, dY \tag{7}$$

Finally, equilibrium equations for different ε terms are given as follows

$$\text{microscale} \quad \left(\varepsilon^{-2}\right) \quad \sigma_{ij,z_j}^{micro}(x,y,z) = 0 \tag{8}$$

$$\text{mesoscale} \quad \left(\varepsilon^{-1}\right) \quad \sigma_{ij,y_j}^{meso}(x,y) = 0 \tag{9}$$

$$\text{macroscale} \quad \left(\varepsilon^{0}\right) \quad \sigma_{ij,x_j}^{macro}(x) + b_i^{macro} = 0 \tag{10}$$

By explicitly writing out terms in microscale equilibrium equation and using separation of variables technique it follows that

$$\begin{aligned}\sigma_{ij,z_j}^{micro}(x,y,z) &= \left(\mathbb{C}_{ijkl}\left(u^{(0)}_{(k,x_l)}(x) + u^{(1)}_{(k,y_l)}(x,y) + u^{(2)}_{(k,z_l)}(x,y,z)\right)\right)_{,z_j} = \left(\mathbb{C}_{ijkl}(z)\left(\Pi_{klmn} + \varphi^{mn}_{(k,z_l)}(z)\right)\right)_{,z_j}\left(u^{(0)}_{(m,x_n)}(x) + u^{(1)}_{(m,y_n)}(x,y)\right) \\ \because u^{(2)}_{(k,z_l)}(x,y,z) &= \varphi^{mn}_{(k,z_l)}(z)\left(u^{(0)}_{(m,x_n)}(x) + u^{(1)}_{(m,y_n)}(x,y)\right) = \left(\mathbb{C}_{ijkl}\left(z\right)\left(\mathbb{I}_{klmn} + \varphi^{mn}_{(k,z_l)}(z)\right)\right)_{,z_j}\varepsilon_{mn}^{meso}\left(x,y\right) = 0\end{aligned} \tag{11}$$

and therefore

$$\left(\mathbb{C}_{ijkl}(z)\left(\mathbb{I}_{klmn} + \varphi^{mn}_{(k,z_l)}(z)\right)\right)_{,z_j} = 0 \quad \forall \quad \varepsilon_{mn}^{meso}(x,y) \neq 0 \tag{12}$$

where φ_k^{mn} is displacement influence function (similar to two-scale case) over microscale domain. Periodic boundary conditions and normalization condition are given as follows

$$\begin{aligned}&\varphi_k^{mn}(z) = \varphi_k^{mn}(z + kl) \quad \text{on} \quad \partial Z \\ &\iiint_Z \varphi_k^{mn}\, dZ = 0\end{aligned} \tag{13}$$

Stiffness tensor can be derived in a similar manner

$$\begin{aligned}&\sigma_{ij}^{meso}(x,y) = \tfrac{1}{|Z|}\iiint_Z \sigma_{ij}^{micro}(x,y,z)\, dZ \\ &= \frac{1}{|Z|}\iiint_Z \left(\mathbb{C}_{ijkl}\left(u^{(0)}_{(k,x_l)}(x) + u^{(1)}_{(k,y_l)}(x,y) + u^{(2)}_{(k,z_l)}(x,y,z)\right)\right) dZ \\ &= \underbrace{\frac{1}{|Z|}\iiint_Z \left(\mathbb{C}_{ijkl}\left(\mathbb{I}_{klmn} + \varphi^{mn}_{(k,z_l)}\right)\right) dZ}_{\mathbb{E}_{ijmn}}\, \varepsilon_{mn}^{meso}\end{aligned} \tag{14}$$

where $\mathbb{E}_{ijmn}$ is homogenized stiffness tensor on mesoscale. Next, similar steps are followed for Eq. (9) as follows

$$\sigma_{ij,y_j}^{meso}(x,y) = \left(\mathbb{E}_{ijkl}\left(u^{(0)}_{(k,x_l)}(x) + u^{(1)}_{(k,y_l)}(x,y)\right)\right)_{,y_j} \tag{15}$$

$$= \left(\mathbb{E}_{ijkl}(y)\left(\mathbb{I}_{klmn} + \chi^{mn}_{(k,y_l)}(y)\right)\right)_{,y_j}\left(u^{(0)}_{(m,x_n)}(x)\right)$$

$$\because u^{(1)}_{(k,y_l)}(x,y) = \chi^{mn}_{(k,y_l)}(y)\left(u^{(0)}_{(m,x_n)}(x)\right)$$

$$= \left(\mathbb{E}_{ijkl}\left(y\right)\left(\mathbb{I}_{klmn} + \chi^{mn}_{(k,y_l)}(y)\right)\right)_{,y_j}\varepsilon^{macro}_{mn}\left(x\right) = 0$$

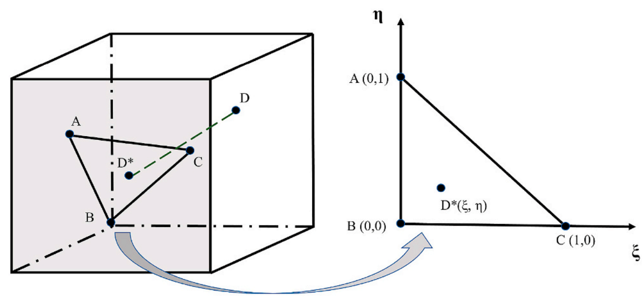

Fig. 11. Imposing PBC for irregular meshes.

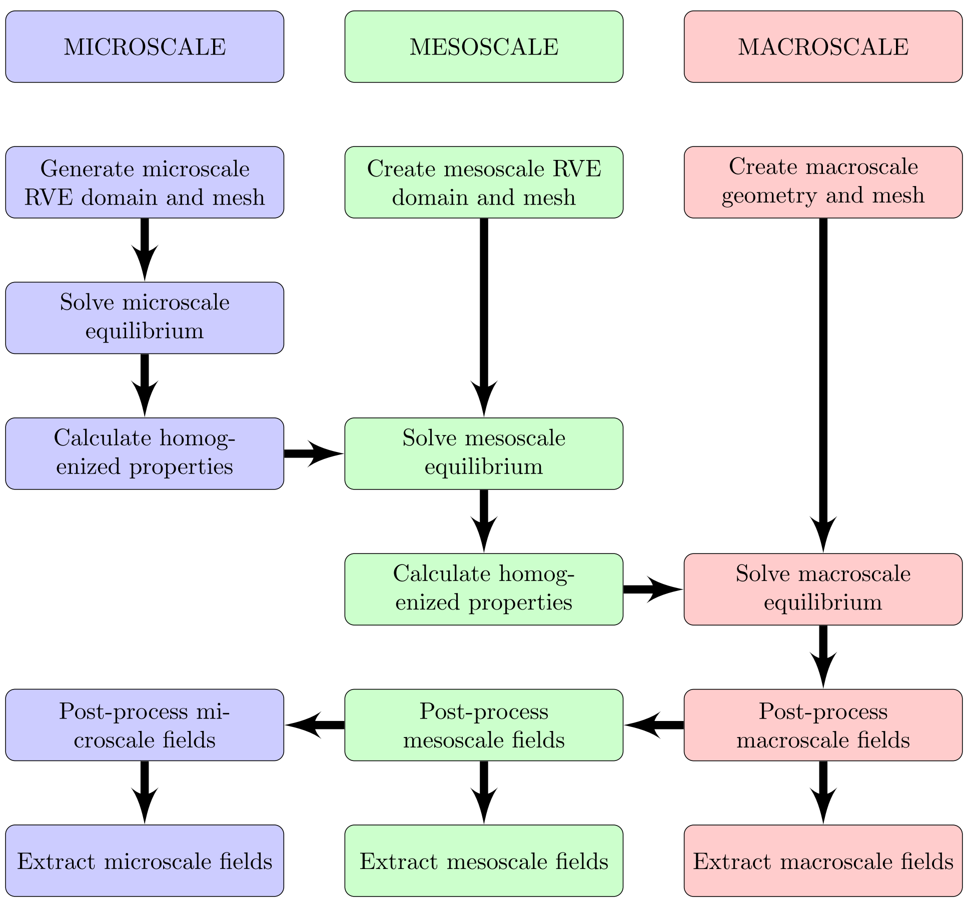

Fig. 12. Three-scale homogenization framework.

Table 7
PLA and SCF properties

Properties	PLA [20]	SCF [2]
Melting Temperature (°C)	215	–
Density ($\frac{g}{cm^3}$)	1.252	1.81
Tensile Strength (MPa)	70	4137
Young Modulus (GPa)	3.5	242
Poisson's Ratio	0.36	0.2

Finally, homogenized properties for macroscale are obtained as follows

$$\begin{aligned}\sigma_{ij}^{macro}(x,y) &= \frac{1}{|Y|}\iiint_Y \sigma_{ij}^{meso}(x,y,z)\,dY \\ &= \frac{1}{|Y|}\iiint_Y \left(\mathbb{E}_{ijkl}\left(u^{(0)}_{(k,x_l)}(x) + u^{(1)}_{(k,y_l)}(x,y)\right)\right) dY \\ &= \underbrace{\frac{1}{|Y|}\iiint_Y \left(\mathbb{E}_{ijkl}\left(\mathbb{I}_{klmn} + \chi^{mn}_{(k,y_l)}\right)\right) dY}_{\mathbb{D}_{ijmn}}\, \varepsilon_{mn}^{macro}\end{aligned} \tag{16}$$

where $\mathbb{D}_{ijmn}$ is homogenized stiffness tensor on macroscale. Eq. A.10 remains the same and is shown below with macroscale boundary conditions.

$$\sigma_{ij,x_j}^{macro}(x) + b_i^{macro} = 0 \quad \text{on} \quad X \tag{17}$$

$$u_i^{(0)} = \tilde{u}_i^{(0)} \quad \text{on} \quad \partial X \tag{18}$$

$$t_i^{(0)} = \tilde{t}_i^{(0)} \quad \text{on} \quad X \tag{19}$$

Shortly summarizing boundary value problems (BVPs), we have

$$\text{Microscale} \quad \left(\mathbb{C}_{ijkl}(z)\left(\mathbb{I}_{klmn} + \varphi^{mn}_{(k,z_l)}(z)\right)\right)_{,z_j} = 0 \quad \text{on} \quad Z \tag{20}$$

$$\varphi_k^{mn}(z) = \varphi_k^{mn}(z + kl) \quad \text{on} \quad \partial Z \tag{21}$$

$$\frac{1}{|Z|}\iiint_Z \varphi_k^{mn}\, dZ = 0 \quad \text{on} \quad Z \tag{22}$$

$$\text{Mesoscale} \quad \left(\mathbb{E}_{ijkl}(y)\left(\mathbb{I}_{klmn} + \chi^{mn}_{(k,y_l)}(y)\right)\right)_{,y_j} = 0 \quad \text{on} \quad Y \tag{23}$$

$$\chi_k^{mn}(y) = \chi_k^{mn}(y + kl) \quad \text{on} \quad \partial Y \tag{24}$$

$$\frac{1}{|Y|}\iiint_Y \chi_k^{mn}\, dY = 0 \quad \text{on} \quad Y \tag{25}$$

$$\text{Macroscale} \quad \sigma_{ij,x_j}^{macro}(x) + b_i^{macro} = 0 \quad \text{on} \quad X \tag{26}$$

$$u_i^{(0)} = \tilde{u}_i^{(0)} \quad \text{on} \quad \partial X \tag{27}$$

$$t_i^{(0)} = \tilde{t}_i^{(0)} \quad \text{on} \quad X \tag{28}$$

$$\text{Mesoscale homogenized stiffness} \quad \mathbb{E}_{ijmn} = \frac{1}{|Z|}\iiint_Z \left(\mathbb{C}_{ijkl}\left(\mathbb{I}_{klmn} + \varphi^{mn}_{(k,z_l)}\right)\right) dZ \tag{29}$$

$$\text{Macroscale homogenized stiffness} \quad \mathbb{D}_{ijmn} = \frac{1}{|Y|}\iiint_Y \left(\mathbb{E}_{ijkl}\left(\mathbb{I}_{klmn} + \chi^{mn}_{(k,y_l)}\right)\right) dY \tag{30}$$

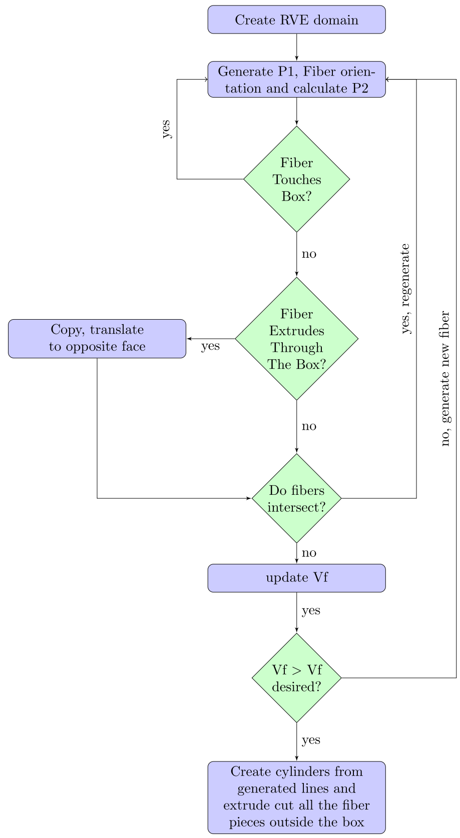

Fig. 13. RVE generation algorithm and framework.

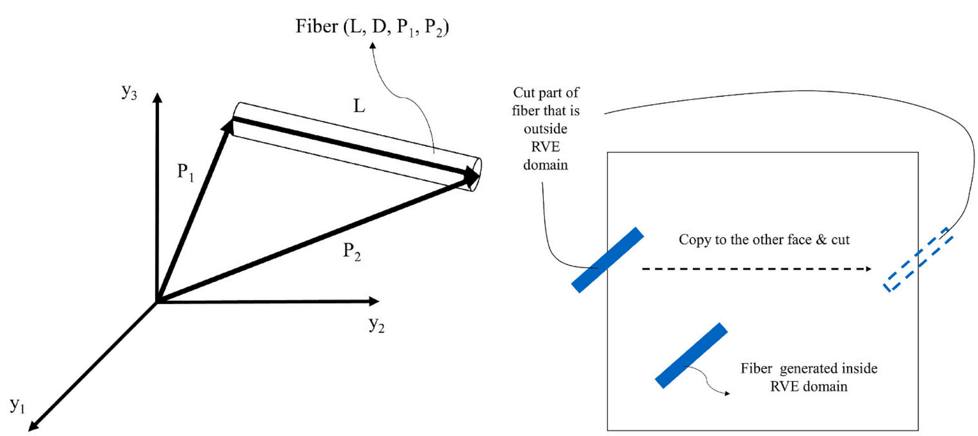

(a) Fiber Parametrization (b) Imposing RVE Periodicity

Fig. 14. RVE Generation a) Fiber parametrization and b) Imposing RVE periodicity.

Finite element method is employed to solve equilibrium PDEs. Since Eq. (22) and Eq. (23) are similar, finite element procedure will be shown on one of them. Multiplying Eq. (23) by test function, w_k , integrating over volume, applying integration by parts and divergence theorem

$$
\begin{aligned}
&\iiint_{\Theta} w_i \mathbb{C}_{ijkl}\left(\mathbb{I}_{klmn} + \chi^{mn}_{(k,y_l)}\right)_{,y_j} d\Theta = \\
&\iiint_{\Theta} \left(w_i \mathbb{C}_{ijkl}\left(\mathbb{I}_{klmn} + \chi^{mn}_{(k,y_l)}\right)\right)_{,y_j} d\Theta + \iiint_{\Theta} w_{i,y_j} \mathbb{C}_{ijkl}\left(\mathbb{I}_{klmn} + \chi^{mn}_{(k,y_l)}\right) d\Theta = \\
&\underbrace{\iiint_{\partial\Theta} w_i \mathbb{C}_{ijkl}\left(\mathbb{I}_{klmn} + \chi^{mn}_{(k,y_l)}\right) n_j^{\Theta}\, d\gamma}_{\left(\mathbb{C}_{ijkl}\left(\mathbb{I}_{klmn} + \chi^{mn}_{(k,y_l)}\right)\right) \text{is anti-periodic on } \partial\Theta} + \iiint_{\Theta} w_{i,y_j} \mathbb{C}_{ijkl}\left(\mathbb{I}_{klmn} + \chi^{mn}_{(k,y_l)}\right) d\Theta = 0
\end{aligned}
\tag{31}
$$

Since boundary integral term vanishes, only volume integral is left. Volume integral is further decomposed into two terms as follows

$$\iiint_{\Theta} w_{i,y_j} \mathbb{C}_{ijmn} d\Theta + \iiint_{\Theta} w_{i,y_j} \mathbb{C}_{ijkl} \chi^{mn}_{(k,y_l)} \, d\Theta = 0 \tag{32}$$

Eq. (32) is the weak form. After deriving weak form, finite element discretization has to be employed. Finite element interpolation of displacement influence function and test function is given below

$$\chi_k^{mn} = \sum_{A=1}^{NNEL} N^A d_k^{mnA} \quad w_k = \sum_{A=1}^{NNEL} N^A c_k^A \tag{33}$$

where *NNEL* is number of nodes per element which is equal to four for linear tetrahedral elements used in this study. Plugging discretized functions into the weak form yields

$$-\sum_{e=1}^{NEL} c_i^A \underbrace{\left[\iiint_{\Theta^e} \frac{\partial N^A}{\partial \xi_I} \frac{\partial \xi_I}{\partial y_j} \mathbb{C}_{ijmn} |\mathbb{J}| \, d\Theta^e\right]}_{F_{f_i}^{mnA}} == \sum_{e=1}^{NEL} c_i^A \underbrace{\left[\iiint_{\Theta^\xi} \frac{\partial N^A}{\partial \xi_I} \frac{\partial \xi_I}{\partial y_j} \mathbb{C}_{ijkl} \frac{\partial N^B}{\partial \xi_J} \frac{\partial \xi_J}{\partial y_l} |\mathbb{J}| \, d\Theta^\xi\right]}_{K_{f_{ik}}^{AB}} d_k^{mnB} \tag{34}$$

where *NEL* is number of elements. Summing matrices over all elements

$$-c_i F_{f_i}^{mn} = c_i K_{f_{ik}} d_k^{mn} \tag{35}$$

$$-F_{f_i}^{mn} = K_{f_{ik}} d_k^{mn} \quad \forall c_i \neq 0 \tag{36}$$

After assembly, boundary conditions have to be applied as well as the normalization condition. In this study, aforementioned conditions are enforced through Lagrangian multipliers. This is accomplished by augmenting stiffness matrix with constraint matrices which contain linear equations that fix specific degrees of freedom (DOFs). Furthermore, solution vector is augmented by Lagrangian multipliers and force vector is augmented by a vector of zeros. Resulting system is shown below

$$\begin{bmatrix} -\boldsymbol{F}_f^{mn} \\ 0 \end{bmatrix} = \begin{bmatrix} \boldsymbol{K}_f & \boldsymbol{B}^T \\ \boldsymbol{B} & 0 \end{bmatrix} \begin{bmatrix} \boldsymbol{d}^{mn} \\ \boldsymbol{\lambda}^{mn} \end{bmatrix} \tag{37}$$

where B is global constraint matrix, K_f is stiffness matrix, F_f^{mn} is global force tensor, d^{mn} is global solution tensor and λ^{mn} is global Lagrangian multiplier tensor. It was found that system above can be solved using LDL^T decomposition from direct methods. Among iterative methods, minimal residual method (MINRES) was applied with diagonal preconditioner [51,58].

In order to solve BVPs, boundary and normalization conditions have to be applied. Although it was discussed that periodic boundary conditions (PBCs) are applied through Lagrangian multipliers, this concept is discussed further in this section. Basically, nodes on opposite planes/faces have to constrained to deform equally. All the vertices are constrained to deform equally while the edges aligned with the same axis are forced to move equally. However, a node on one face does not necessarily have a corresponding node onto the other face with the same planar coordinates. This is typically hard to control in the unstructured meshes. Therefore, nodes on one face are mapped on the opposite face. Mapped nodes are placed in a triangle that is intersection between tetrahedral element and boundary of RVE. Since coordinates of the nodes are known, the triangle is mapped to ideal coordinates as illustrated in Fig. 11. Then, a value for a variable χ at node D is interpolated between A, B, and C as shown in equation below

$$\chi_k^{mnD} = \chi_k^{mnA} \xi + \chi_k^{mnB} (1-\xi)(1-\eta) + \chi_k^{mnC} \eta \tag{38}$$

where ξ and η are calculated using equation below

$$\begin{bmatrix} x^D - x^B \\ y^D - y^B \end{bmatrix} = \begin{bmatrix} x^A - x^B & x^C - x^B \\ y^A - y^B & y^C - y^B \end{bmatrix} \begin{bmatrix} \xi \\ \eta \end{bmatrix} \tag{39}$$

In order to form constraint matrix, terms in Eq. (38) have to be moved to the right hand side and constants in front of corresponding χ_k^{mn} terms have to recorded in the matrix. In other words, the following equation shows the constraint equation for a sample slave node D imposed in the constraint matrix

$$\lambda_k^{mnD} \left(-\chi_k^{mnD} + \chi_k^{mnA} \xi + \chi_k^{mnB} (1-\xi)(1-\eta) + \chi_k^{mnC} \eta \right) = 0 \tag{40}$$

where λ is Lagrangian multiplier corresponding to the number of constraint equation. Eq. (40) is appended to the constraint matrix B with global node numbers instead of the local ones. There are as many equations appended as many degrees of freedom on the slave face. Eq. (22) is imposed using Lagrangian multipliers and by breaking up the integral into set of linear equations using shape functions as shown below:

$$\lambda_k \sum_{EL=1}^{NEL} \left(\frac{1}{|Z|} \iiint_Z \sum_{A=1}^{NNEL} N^A \varphi_k^{mn^A} \, dZ \right) = 0 \tag{41}$$

φ is discretized over the element and interpolated using shape functions N, then equation is integrated over the element using isoparametric mapping. Then, for each m and n there will be three equations to impose, due to the index k. These equations were appended to constraint matrix B with global degrees of freedom replacing the local ones.

Overall procedure is illustrated in Fig. 12. The macroscale and RVE geometries are generated in SolidWorks and FreeCAD, and meshed in ANSYS. Mesoscale and microscale RVEs were meshed with linear tetrahedral elements and macroscale specimen was meshed with linear hexahedral elements. Mesoscale ideal 0 and 0/90 RVEs were meshed with 43483 and 86870 elements. Mesoscale actual 0 and 0/90 RVEs were meshed with 77073 and

155536 elements. Microscale random 5%, 7.5% and 10% RVEs were meshed with 996552, 1098529 and 1288091 elements. Microscale aligned 5%, 7.5% and 10% RVEs were meshed with 159631, 201867 and 243367 elements. Mesh refinement procedure was carried out at each homogenization case and stopped when difference between obtained modulus values was less than 1%. Generated mesh was imported in MATLAB where all of the discussed PDEs and post-processing steps were carried out. Finally, FEM results are exported to Paraview to visualize obtained results such as deformation, strain and stress fields [60]. It should be noted that fiber-matrix interface was assumed to be perfect and, therefore, nodes on the fiber-matrix interface were merged.

B. Microscale RVE Generation

The fiber generation algorithm used in this research is shown in Fig. 13. P_1 and P_2 are vectors defining the position of the fiber in space as shown in Fig. 14a. In this study, the length was assumed to be equal to the average length and the diameter was assumed to be equal to the nominal diameter of the fibers. Periodicity was imposed by copying and translating fibers that cross the RVE boundary accross the RVE length. Then part of fibers that cross RVE boundary are cut. This concept is illustrated in Fig. 14b. It is obvious that if RVE is copied and translated by its size then two fiber pieces will generate a full fiber thus ensuring periodicity.

Last important concept in the algorithm is checking for the fiber-to-fiber intersection. This is done by calculating minimum distance between two fibers and comparing it to the fiber diameter. If the distance is smaller than the fiber diameter then fibers intersect and a new fiber has to be generated. The algorithm for calculating minimum distance between two line segments is described in detail by Eberly [19]. The MATLAB code for this problem is given in Ref. [1] and is adopted in this research to measure fiber-to-fiber intersection.

$$\mathbb{D}^{random} = \begin{bmatrix} 6.893*10^9 & SYM & SYM & SYM & SYM & SYM \\ 3.576*10^9 & 6.801*10^9 & SYM & SYM & SYM & SYM \\ 3.557*10^9 & 3.573*10^9 & 6.774*10^9 & SYM & SYM & SYM \\ 1.005*10^6 & -3.788*10^7 & -4.695*10^7 & 1.694*10^9 & SYM & SYM \\ 6.629*10^7 & 3.378*10^7 & 6.267*10^7 & 2.228*10^7 & 1.670*10^9 & SYM \\ -1.262*10^6 & 2.763*10^6 & 2.484*10^7 & 4.039*10^7 & -2.145*10^5 & 1.705*10^9 \end{bmatrix} \tag{42}$$

$$\mathbb{D}^{aligned} = \begin{bmatrix} 6.297*10^9 & SYM & SYM & SYM & SYM & SYM \\ 3.438*10^9 & 6.303*10^9 & SYM & SYM & SYM & SYM \\ 3.440*10^9 & 3.449*10^9 & 9.107*10^9 & SYM & SYM & SYM \\ -8.570*10^5 & 1.159*10^6 & 1.327*10^6 & 1.458*10^9 & SYM & SYM \\ -8.966*10^5 & -6.579*10^5 & -3.336*10^6 & 3.842*10^6 & 1.452*10^9 & SYM \\ 4.368*10^6 & 3.304*10^6 & 3.139*10^6 & 2.371*10^5 & -5.531*10^5 & 1.433*10^9 \end{bmatrix} \tag{43}$$

References

[1] Shortest. Distance between two line segments. URL: https://www.mathworks.com/matlabcentral/fileexchange/32487-shortest-distance-between-two-line-segments.

[2] Zoltek Px 35. URL: https://zoltek.com/products/px35/.

[3] Advani SG, Tucker CL. The use of tensors to describe and predict fiber orientation in short fiber composites. J Rheol 1987;31:751–84. https://doi.org/10.1122/1.549945.

[4] Ahn SH, Montero M, Odell D, Roundy S, Wright PK. Anisotropic material properties of fused deposition modeling ABS. Rapid Prototyp J 2002;8:248–57. https://doi.org/10.1108/13552540210441166.

[5] Babu K, Mohite P, Upadhyay C. Development of an RVE and its stiffness predictions based on mathematical homogenization theory for short fibre composites. Int J Solid Struct 2018;130–131:80–104. https://doi.org/10.1016/j.ijsolstr.2017.10.011.

[6] Belhouideg S. Prediction of effective mechanical properties of composite materials using homogenization approach: application to tungsten fiber reinforced bulk metallic glass matrix composite. European Mechanical Science 2018;2:68–75. https://doi.org/10.26701/ems.376369.

[7] Bhate D. Constitutive modeling of 3d printed fdm parts: Part 1 (challenges) – padt, inc. – the blog. URL: http://www.padtinc.com/blog/constitutive-modeling-of-3d-printed-fdm-parts/. Accessed on 11/01/2019.

[8] Biswas P, Guessasma S, Li J. Numerical prediction of orthotropic elastic properties of 3d-printed materials using micro-CT and representative volume element. Acta Mech 2019. https://doi.org/10.1007/s00707-019-02544-2.

[9] Bouaoune L, Brunet Y, el moumen A, Kanit T, Mazouz H. Random versus periodic microstructures for elasticity of fibers reinforced composites. Compos B Eng 2016;103. https://doi.org/10.1016/j.compositesb.2016.08.026.

[10] Brenken B, Barocio E, Favaloro A, Kunc V, Pipes RB. Fused filament fabrication of fiber-reinforced polymers: a review. Additive Manufacturing 2018;21:1–16. https://doi.org/10.1016/j.addma.2018.01.002.

[11] Conner BP, Manogharan GP, Martof AN, Rodomsky LM, Rodomsky CM, Jordan DC, Limperos JW. Making sense of 3-d printing: creating a map of additive manufacturing products and services. Additive Manufacturing 2014;1–4:64–76. https://doi.org/10.1016/j.addma.2014.08.005.

[12] Croccolo D, De Agostinis M, Olmi G. Experimental characterization and analytical modelling of the mechanical behaviour of fused deposition processed parts made of ABS-M30. Comput Mater Sci 2013;79:506–18. https://doi.org/10.1016/J.COMMATSCI.2013.06.041. URL: https://www.sciencedirect.com/science/article/pii/S0927025613003741.

[13] Cuan-Urquizo E, Barocio E, Tejada-Ortigoza V, Pipes R, Rodriguez C, Roman-Flores A. Characterization of the mechanical properties of {FFF} structures and materials: a review on the experimental, computational and theoretical approaches. Materials 2019;12:895. https://doi.org/10.3390/ma12060895.

[14] Curran S, Chambon P, Lind R, Love L, Wagner R, Whitted S, Smith D, Post B, Graves R, Blue C, et al. Big area additive manufacturing and hardware-in-the-loop for rapid vehicle powertrain prototyping: a case study on the development of a 3-D-printed Shelby Cobra. 2016. Technical Report. SAE Technical Paper.

[15] Domingo-Espin M, Puigoriol-Forcada JM, Garcia-Granada AA, Llumà J, Borros S, Reyes G. Mechanical property characterization and simulation of fused deposition modeling Polycarbonate parts. Mater Des 2015;83:670–7. https://doi.org/10.1016/j.matdes.2015.06.074.

[16] Dutra TA, Ferreira RTL, Resende HB, Guimarães A. Mechanical characterization and asymptotic homogenization of 3d-printed continuous carbon fiber-reinforced thermoplastic. J Braz Soc Mech Sci Eng 2019;41. https://doi.org/10.1007/s40430-019-1630-1.

[17] Duty C, Failla J, Kim S, Smith T, Lindahl J, Kunc V. Z-pinning approach for 3d printing mechanically isotropic materials. Additive Manufacturing 2019;27:175–84. https://doi.org/10.1016/j.addma.2019.03.007.

[18] E. Cuan-Urquizo, A. B, . Micromechanics of additively manufactured structures: computational and laboratory experiments .

[19] Eberly D. Robust computation of distance between line segments. 2015.

[20] Farah S, Anderson DG, Langer R. Physical and mechanical properties of {PLA}, and their functions in widespread applications {\textemdash} A comprehensive review. Adv Drug Deliv Rev 2016;107:367–92. https://doi.org/10.1016/j.addr.2016.06.012.

[21] Fidan I, Imeri A, Gupta A, Hasanov S, Nasirov A, Elliott A, Alifui-Segbaya F, Nanami N. The trends and challenges of fiber reinforced additive manufacturing. Int J Adv Manuf Technol 2019. https://doi.org/10.1007/s00170-018-03269-7. URL: http://link.springer.com/10.1007/s00170-018-03269-7.

[22] Fish J. Practical multiscaling. John Wiley & Sons; 2013. https://www.ebook.de/de/product/20764120/jacob{_}fish{_}j{_}fish{_}fish{_}practical{_}multiscaling.html.

[23] Goh GD, Yap YL, Agarwala S, Yeong WY. Recent progress in additive manufacturing of fiber reinforced polymer composite. Advanced Materials Technologies 2018;4:1800271. https://doi.org/10.1002/admt.201800271.

[24] Guedes J, Kikuchi N. Preprocessing and postprocessing for materials based on the homogenization method with adaptive finite element methods. Comput Methods

Appl Mech Eng 1990;83:143–98. https://doi.org/10.1016/0045-7825(90)90148-F. URL: https://linkinghub.elsevier.com/retrieve/pii/004578259090148F.
[25] Gupta A, Fidan I, Hasanov S, Nasirov A. Processing, mechanical characterization, and micrography of 3d-printed short carbon fiber reinforced polycarbonate polymer matrix composite material. Int J Adv Manuf Technol 2020;107:3185–205. https://doi.org/10.1007/s00170-020-05195-z.
[26] Gupta A, Hasanov S, Fidan I. Processing and characterization of 3D printed polymer matrix composites reinforced with discontinuous fibers. In: Proceedings of the 30th annual international solid freeform fabrication symposium-an additive manufacturing conference, austin, TX; 2019.
[27] Gupta M, Wang KK. Fiber orientation and mechanical properties of short-fiber-reinforced injection-molded composites: simulated and experimental results. Polym Compos 1993;14:367–82.
[28] Hassani B, Hinton E. Homogenization and structural topology optimization. London: Springer London; 1999. https://doi.org/10.1007/978-1-4471-0891-7. URL: http://link.springer.com/10.1007/978-1-4471-0891-7.
[29] Heller, B., Smith, D., Jack, D., . Effect of extrudate swell, nozzle shape, and convergence zone on fiber orientation in fused deposition modeling nozzle flow .
[30] Heller BP, Smith DE, Jack DA. Effects of extrudate swell and nozzle geometry on fiber orientation in fused filament fabrication nozzle flow. Additive Manufacturing 2016;12:252–64. https://doi.org/10.1016/j.addma.2016.06.005.
[31] Imeri A, Fidan I, Allen M, Wilson DA, Canfield S. Fatigue analysis of the fiber reinforced additively manufactured objects. Int J Adv Manuf Technol 2018;98: 2717–24. https://doi.org/10.1007/s00170-018-2398-7.
[32] Islam M, Begum K. Prediction models for the elastic modulus of fiber-reinforced polymer composites: an analysis. J Sci Res 2011;3:225–38.
[33] Kamiński M. Multiscale homogenization of n-component composites with semi-elliptical random interface defects. Int J Solid Struct 2005;42:3571–90. https://doi.org/10.1016/j.ijsolstr.2004.11.001.
[34] Kanouté P, Boso DP, Chaboche JL, Schrefler BA. Multiscale methods for composites: a review. Arch Comput Methods Eng 2009;16:31–75. https://doi.org/10.1007/s11831-008-9028-8.
[35] Klosterman D, Chartoff R, Graves G, Osborne N, Priore B. Interfacial characteristics of composites fabricated by laminated object manufacturing. Compos Appl Sci Manuf 1998;29:1165–74. https://doi.org/10.1016/s1359-835x(98)00088-8.
[36] Kruth JP, Mercelis P, Vaerenbergh JV, Froyen L, Rombouts M. Binding mechanisms in selective laser sintering and selective laser melting. Rapid Prototyp J 2005;11: 26–36. https://doi.org/10.1108/13552540510573365.
[37] Li L, Sun Q, Bellehumeur C, Gu P. Composite modeling and analysis for fabrication of {FDM} prototypes with locally controlled properties. J Manuf Process 2002;4: 129–41. https://doi.org/10.1016/s1526-6125(02)70139-4.
[38] Melchels FP, Feijen J, Grijpma DW. A review on stereolithography and its applications in biomedical engineering. Biomaterials 2010;31:6121–30. https://doi.org/10.1016/j.biomaterials.2010.04.050.
[39] Mohammadizadeh M, Fidan I, Allen M, Imeri A. Creep behavior analysis of additively manufactured fiber-reinforced components. Int J Adv Manuf Technol 2018;99:1225–34. https://doi.org/10.1007/s00170-018-2539-z.
[40] el moumen A, Imad A, Kanit T, Hilali E, Minor H. A multiscale approach and microstructure design of the elastic composite behavior reinforced with natural particles. Compos B Eng 2014;66:247–54. https://doi.org/10.1016/j.compositesb.2014.05.008.
[41] Moumen AE, Tarfaoui M, Lafdi K. Additive manufacturing of polymer composites: processing and modeling approaches. Compos B Eng 2019;171:166–82. https://doi.org/10.1016/j.compositesb.2019.04.029.
[42] Nasirov A, Fidan I. Prediction of mechanical properties of fused filament fabricated structures via asymptotic homogenization. Mech Mater 2020;145:103372. https://doi.org/10.1016/j.mechmat.2020.103372.
[43] Nasirov A, Hasanov S, Fidan I. Prediction of mechanical properties of fused deposition modeling made parts using multiscale modeling and classical laminate theory. In: Proceedings of the 30th annual international solid freeform fabrication symposium-an additive manufacturing conference, austin, TX; 2019.
[44] Ngo T, Ghazlan A, Hui D. Bimaterial 3d printing and numerical analysis of bio-inspired composite structures under in-plane and transverse loadings. Compos B Eng 2016;108. https://doi.org/10.1016/j.compositesb.2016.09.083.
[45] Ngo TD, Kashani A, Imbalzano G, Nguyen KTQ, Hui D. Additive manufacturing (3D printing): a review of materials, methods, applications and challenges. Compos B Eng 2018;143:172–96. https://doi.org/10.1016/j.compositesb.2018.02.012.
[46] Ortolano González JM, Hernández Ortega JA, Oliver Olivella X. A comparative study on homogenization strategies for multi-scale analysis of materials. Centre Internacional de Mètodes Numèrics en Enginyeria (CIMNE); 2013.
[47] Papon EA, Haque A, Mulani S. Process optimization and stochastic modeling of void contents and mechanical properties in additively manufactured composites. Compos B Eng 2019;107325doi. https://doi.org/10.1016/j.compositesb.2019.107325.
[48] Park C, Jung J, Yun G. Thermomechanical properties of mineralized nitrogen-doped carbon nanotube/polymer nanocomposites by molecular dynamics simulations. Compos B Eng 2019;161. https://doi.org/10.1016/j.compositesb.2019.01.002.
[49] Ramírez-Torres A, Penta R, Rodríguez-Ramos R, Merodio J, Sabina FJ, Bravo-Castillero J, Guinovart-Díaz R, Preziosi L, Grillo A. Three scales asymptotic homogenization and its application to layered hierarchical hard tissues. Int J Solid Struct 2018;130–131:190–8. https://doi.org/10.1016/j.ijsolstr.2017.09.035.
[50] Rodríguez JF, Thomas JP, Renaud JE. Mechanical behavior of acrylonitrile butadiene styrene fused deposition materials modeling. Rapid Prototyp J 2003;9: 219–30.
[51] Saad Y. Iterative methods for sparse linear systems, vol. 82. siam; 2003.
[52] Sanchez-Palencia, E., . Homogenization in mechanics. A survey of solved and open problems .
[53] Sokołowski D, Kamiński M. Homogenization of carbon/polymer composites with anisotropic distribution of particles and stochastic interface defects. Acta Mech 2018;229:3727–65. https://doi.org/10.1007/s00707-018-2174-7.
[54] Somireddy M, Czekanski A, Singh CV. Development of constitutive material model of 3D printed structure via FDM. Materials Today Communications 2018;15: 143–52. https://doi.org/10.1016/j.mtcomm.2018.03.004. https://linkinghub.elsevier.com/retrieve/pii/S2352492818300552.
[55] Somireddy M, Singh C, Czekanski A. Mechanical behaviour of 3d printed composite parts with short carbon fiber reinforcements. Eng Fail Anal 2020;107: 104232. https://doi.org/10.1016/j.engfailanal.2019.104232.
[56] Thomas KL, Bryce HCA, Heitzmann MT. Generation of a short fibre biocomposite representative volume element. 2015.
[57] Wang Z, Smith D. Rheology effects on predicted fiber orientation and elastic properties in large scale polymer composite additive manufacturing. Journal of Composites Science 2018;2:10. https://doi.org/10.3390/jcs2010010.
[58] Wathen AJ. Preconditioning. Acta Numer 2015;24:329–76.
[59] Yang Z, Ren W, Sharma R, McDonald S, Mostafavi M, Vertyagina Y, Marrow TJ. In-situ X-ray computed tomography characterisation of 3D fracture evolution and image-based numerical homogenisation of concrete. Cement Concr Compos 2017; 75:74–83. https://doi.org/10.1016/j.cemconcomp.2016.10.001.
[60] Yeh C. Export FEM results in VTK file format. accessed October 27, 2019. 2016. https://github.com/joe-of-all-trades/vtkwrite/blob/master/vtkwrite.m.
[61] Yuan Z, Fish J. Toward realization of computational homogenization in practice. Int J Numer Methods Eng 2008;73:361–80. https://doi.org/10.1002/nme.2074. URL: http://doi.org/10.1002/nme.2074.
[62] Zerhouni O, Tarantino M, Danas K. Numerically-aided 3d printed random isotropic porous materials approaching the hashin-shtrikman bounds. Compos B Eng 2018; 156. https://doi.org/10.1016/j.compositesb.2018.08.032.